

Article

# A Spectral Wave Model for Inhomogeneous Water Wave Fields Using the Quasi-Coherent Theory

Vasilis Baltikas  and Yannis N. Krestenitis \* 

Laboratory of Maritime Engineering and Maritime Works, School of Civil Engineering, Aristotle University of Thessaloniki, GR-54124 Thessaloniki, Greece; vmpaltik@civil.auth.gr

\* Correspondence: ynkrest@civil.auth.gr

**Abstract:** A numerical stochastic wave model was developed in this study based on the quasi-coherent theoretical framework proposed by Smit and Janssen in 2013. Subsequently, the model was implemented to reproduce and cross-confirm the findings of the quasi-coherent (QC) spectral wave modeling approach. The process included simulations of experiments conducted by Vincent and Briggs regarding waves propagating over a submerged shoal. The results of the simulations agree with the expected results of the QC theory, which can account for the spatial coherence of inhomogeneous wave fields and capture wave interference more accurately than conventional spectral wave models. In addition, extra insight was gained about aspects of the overall numerical implementation of the QC theory.

**Keywords:** ocean waves; spectral wave modeling; inhomogeneous wave fields; wave interference; quasi-coherent theory; wave model

## 1. Introduction

Stochastic, spectral, or phase-averaged wave models are the most used terms that describe a family of wave models that simulate the generation of random sea waves, as well as the evolution of the generated wave fields in space and time, due to various processes that occur as the waves propagate in a variable medium [1–3]. Regardless of their specific differences, these models are built around the radiative transfer equation (RTE), which is expressed as:

$$\partial_t E + c_k \nabla_k E + c_x \nabla_x E = 0 \quad (1)$$

$$\partial_t E + c_\sigma \nabla_\sigma E + c_\theta \nabla_\theta E + c_x \nabla_x E = 0 \quad (2)$$

Equations (1) and (2) describe the local change in a wave's energy or action over time and their transport in geographical and spectral space.  $E(\mathbf{k}, \mathbf{x}, t)$  or  $E(\sigma, \theta, \mathbf{x}, t)$  represents the well-known wave energy or action variance density spectrum at a point ( $\mathbf{x} = [x, y]$ ) in geographical space, expressed either in terms of the wavenumber ( $\mathbf{k} = [k_x, k_y]$ ) spectral space or frequency–direction ( $\sigma, \theta$ ) spectral space. Respectively,  $c_x = [c_x, c_y]$ ,  $c_k = [c_{kx}, c_{ky}]$  and  $c_\sigma, c_\theta$  are the matching geographical and spectral transport velocities.

Using the RTE as the basis of spectral wave models presupposes the assumption that wave fields can be described as quasi-homogeneous and Gaussian random processes. This hypothesis may be held in open sea waters, where wave statistics undergo slow variations on a spatial scale of hundreds to thousands of wave lengths, but this is not the case as waves approach the shore. There, the more intense effects of medium variations on the wave propagation (e.g., topography) and the weaker dispersive behavior of the waves in shallow waters can cause deviations from the above. These “deviations” are statistical representations of wave interference patterns (e.g., in focal zones), the spatial coherence and cross-correlations of the wave field, which are more evident in shallow waters. The



**Citation:** Baltikas, V.; Krestenitis, Y.N. A Spectral Wave Model for Inhomogeneous Water Wave Fields Using the Quasi-Coherent Theory. *J. Mar. Sci. Eng.* **2023**, *11*, 2066. <https://doi.org/10.3390/jmse11112066>

Academic Editor: Jinyu Sheng

Received: 31 July 2023

Revised: 24 September 2023

Accepted: 25 October 2023

Published: 29 October 2023



**Copyright:** © 2023 by the authors. Licensee MDPI, Basel, Switzerland. This article is an open access article distributed under the terms and conditions of the Creative Commons Attribution (CC BY) license (<https://creativecommons.org/licenses/by/4.0/>).

RTE is not able to account for these deviations, as its derivation is based on the evolution of the auto-covariance function of the sea surface, where the Fourier transform of the latter yields the variance density spectrum.

Despite the drawbacks mentioned previously, RTE-based spectral wave models have been successfully used to simulate the generation and propagation of random ocean waves in stand-alone small- and large-scale applications [4–7] and as components of sea-state forecast platforms [8–12]. The suitability of RTE spectral wave models for modeling sea waves is based on the fact that the hypotheses of homogeneous wave fields and Gaussian statistics hold for the greater part of the ocean and the open seas. Moreover, the isotropic and advection-like formalism of the RTE equation make its numerical evaluation possible with a variety of methods, implicit and explicit, on both structured and unstructured computational grids [2,3]. Over the years, the operational use of RTE-based spectral wave models has been extended by the inclusion of wave–current interactions, the development and addition of various source terms on the RHS that mainly account for air–sea-surface interactions and the generation of wind waves, non-conservative processes (e.g., white-capping, depth-induced wave breaking, bottom friction, etc.) and the approximation of non-linear wave–wave interactions (quadruplets and triads) [13–15].

The greater part of the continuous development of spectral wave models has remained within the confines of the classic RTE physics and theoretical framework. The evaluation of wave fields, while accounting for spatial coherency, cross-correlations and the interference of wave components (shallow waters, interaction with coastal structures, etc.), is commonly reserved for deterministic phase-resolving models, usually Boussinesque-type models or those based on some form or solution of either the mild slope equation or the shallow water equations, and lately, 3D or quasi-3D Navier–Stokes and non-hydrostatic models have been proposed [16–26].

Alongside the development and operational extension of classic spectral wave models, advances have also been made in modeling inhomogeneous ocean waves. However, almost all the proposed models do not match the ability of classic RTE-based models when used as almost general-purpose spectral wave models for simulating the evolution of wave fields through a slowly varying medium, regardless of the width and directional distribution of the wave variance density spectra. They are restricted to special cases due to restrictions imposed by assumptions, mainly regarding the dimensionality of the bathymetry and its variations or focusing on wave fields with a narrow bandwidth [27–34].

Building upon previous efforts and using mathematical tools and concepts from other scientific disciplines, such as quantum optics, Smit and Janssen [35] presented a generalization of the theoretical framework of spectral wave models such that modeling of inhomogeneous wave fields can be achieved within the wider scope of the linear waves theory, without the previous restrictions. Their approach is based on replacing the evolution of the auto-covariance function of the sea surface with the evolution of the covariance function, thus considering the contributions of the cross-correlations responsible for wave interference. As a result, they also introduced the more general coupled-mode spectrum, which can capture coherent interference effects, replacing the classic variance density spectrum.

The main result of Smit and Janssen [35] consists of the following two equations, which can describe the evolution of the second-order wave statistics of inhomogeneous wave fields, including spatial coherency and wave interference:

$$\begin{aligned} \partial_t W(\mathbf{k}, \mathbf{x}, t) = & -i \int_{\mathbf{D}} \widehat{\Omega}^{(N)}\left(\mathbf{k} - \frac{i}{2} \nabla_{\mathbf{x}}, \mathbf{q}\right) W\left(\mathbf{k} - \frac{1}{2} \mathbf{q}, \mathbf{x}\right) \exp(i\mathbf{q} \cdot \mathbf{x}) \\ & + i \int_{\mathbf{D}} \widehat{\Omega}^{(N)}\left(\mathbf{k} + \frac{i}{2} \nabla_{\mathbf{x}}, \mathbf{q}\right) W\left(\mathbf{k} + \frac{1}{2} \mathbf{q}, \mathbf{x}\right) \exp(-i\mathbf{q} \cdot \mathbf{x}) \end{aligned} \tag{3}$$

$$\widehat{\Omega}^{(N)}\left(\mathbf{k} - \frac{i}{2} \nabla_{\mathbf{x}}, \mathbf{q}\right) = \sum_{|n|=0}^N \frac{1}{n!} \left(-\frac{i}{2}\right)^{|n|} \frac{\partial^n \sigma}{\partial \mathbf{k}^n} \frac{\partial^n}{\partial \mathbf{x}^n} \tag{4}$$

Equation (3) is an integrodifferential equation that describes the evolution of the coupled-mode spectrum,  $W$ , in spectral space, geographical space and time while considering spatial coherence and wave interference over a domain,  $\mathbf{D}$ . The variable  $\mathbf{q}$  in Equations (3) and (4) represents a lag in the wavenumber space and is the Fourier conjugate of  $\mathbf{x}$ . Equation (4) yields the integral's kernel,  $\widehat{\Omega}^{(N)}$ , which is a pseudo-differential operator associated with the linear wave theory dispersion relation. The derivation of the above expressions includes the use of the Weyl association rule and pseudo-differential operator algebra [36,37]. Specifically, Equation (4) gives the  $N$ -th-order approximation of the kernel, referred to as its  $N$ -th-order quasi-coherent approximation. The specifics of the derivation process are presented in [35], alongside the relation of Equation (3) with other transport equations of wave statistics, which are proven to be special cases of the former, including the RTE.

Smit et al. [38] presented how the first-order approximation of Equation (3) can be cast in a form resembling the RTE, including an extra scattering term that accounts for the generation and transport of spatial coherency, cross-correlations and wave interference in the wave field. Subsequently, Smit et al. [39] presented a framework for developing wave energy dissipation source terms, adding a suitable depth-induced wave breaking term. Akrish et al. [40,41] extended the derived QC model with the inclusion of wave–current interactions and have recently shown the application of the Weyl association rule to the study of water wave propagation while also supplying a more formal derivation of the RTE and its QC generalization.

In the present paper, we present our version of the first-order QC spectral wave model based on the work of Smit and Janssen [35] and Smit et al. [38,39]. The paper contains brief presentations of the core equations and the numerical scheme we employed. We validated our model against data from the laboratory experiments of Vincent and Briggs [42], obtained by observations of waves propagating over a submerged elliptic shoal. The presented test cases included both the ones considered by Smit and Janssen [35] as well as additional ones. The purpose of the former was to present that our version of the model reproduced the key findings of the QC theory while also cross-validating our chosen set-up of the model against the already published results of Smit and Janssen's [35] simulations. The comparisons of our model's results against observational data from more test cases from Vincent and Briggs [42] served the purpose further validating our QC model.

This work is part of a wider research project, which aims to explore the potential of the QC theoretical framework in its current state and towards more operational use cases while also creating an additional testing environment for the QC theory with the ambition of contributing to its development in the future. Another goal of our research is to examine various aspects of the overall behavior and performance of a numerical spectral wave model based on the QC theory.

## 2. Materials and Methods

### 2.1. The Numerical Model

#### 2.1.1. Model Equations

We implemented the QC theoretical framework in a numerical spectral wave model built from the ground up and coded into a computer program using the Fortran programming language. This was a more straightforward approach to implementing the core of the theory, which was used instead of modifying existing open-source software of spectral wave models, which would, at that time, have required addressing issues regarding their code structure. The most recent versions of the SWAN wave model have gradually included the option of QC wave modeling. However, to the best of our knowledge, there are no published applications of QC modeling with SWAN, at least up to this paper's submission.

The model's governing equation is the first-order quasi-coherent approximation of Equation (3), cast in a form like the classic RTE [38]:

$$\partial_t W + \mathbf{c}_k \nabla_k W + \mathbf{c}_x \nabla_x W = S_{qc} \quad (5)$$

As mentioned earlier,  $W(\mathbf{k}, \mathbf{x}, t)$  is not the regular wave variance density spectrum, but the more general coupled-mode spectrum. The definition of  $W(\mathbf{k}, \mathbf{x}, t)$  is given by the following Fourier transform expression:

$$W(\mathbf{k}, \mathbf{x}, t) = \bar{F}_{\xi, \mathbf{k}}[\Gamma(\xi, \mathbf{x}, t)] = \frac{1}{(2\pi)^2} \int \Gamma(\xi, \mathbf{x}, t) \exp(-i\mathbf{k}\xi) d\xi \tag{6}$$

$$\Gamma(\xi, \mathbf{x}, t) = \frac{1}{2} \left\langle \left( \mathbf{x} + \frac{\xi}{2}, t \right) \zeta^* \left( \mathbf{x} - \frac{\xi}{2}, t \right) \right\rangle \tag{7}$$

$\Gamma(\xi, \mathbf{x}, t)$  is the covariance function of a complex, Gaussian and zero-mean variable,  $\zeta(\mathbf{x}, t)$ , which is associated with the real-valued surface elevation  $\eta(\mathbf{x}, t) = \text{Re} [\zeta(\mathbf{x}, t)]$  between two geographical space points  $\mathbf{x} + \xi/2, \mathbf{x} - \xi/2$ . The imaginary part of  $\zeta(\mathbf{x}, t)$  is the Hilbert transform pair of its real part. The relationship between  $\eta(\mathbf{x}, t)$  and  $\zeta(\mathbf{x}, t)$  is the equivalent of the one between the real and its complex analytic signal, which was introduced in signal processing by Gabor [43] and was later used in quantum optics [44]. The vector  $\xi$  denotes a spatial separation or lag distance within a decorrelation length scale  $\xi_c = 2\pi/\Delta k_0$  [38,39], such that when  $|\xi|$  approaches  $\xi_c$ , the wave field components decorrelate and  $\Gamma(\xi, \mathbf{x}, t)$  vanishes. Here,  $\Delta k_0$  denotes a representative width of the incident spectrum.

The above expressions show that the CM spectrum  $W(\mathbf{k}, \mathbf{x}, t)$  is, in essence, a Wigner–Ville distribution [45,46]. It describes the complete second-order statistics of the wave field, accounting for its coherence and providing a more accurate stochastic representation of wave interference. The CM spectrum may reduce to the variance density spectrum, where the wave field is quasi-homogeneous (e.g.,  $\xi_c \rightarrow 0$ ).  $W(\mathbf{k}, \mathbf{x}, t)$  cannot be directly interpreted as a variance density spectrum, nor can it be related to the wave energy of a specific wave component at a given point in geographical space, since the Wigner–Ville distribution can take negative values. However, it is possible to obtain the local variance density by using the marginal properties of the Wigner distribution:

$$E(\mathbf{x}, t) = \int W(\mathbf{k}, \mathbf{x}, t) d\mathbf{k}, \quad E(\mathbf{k}, t) = \int W(\mathbf{k}, \mathbf{x}, t) d\mathbf{x} \tag{8}$$

The transport velocities in Equation (5) are defined as  $\mathbf{c}_k = -\nabla_x \sigma, \mathbf{c}_x = \frac{\mathbf{k}}{|\mathbf{k}|} \nabla_k \sigma$  and are derived from the linear wave theory dispersion relation  $\sigma = \sqrt{g|\mathbf{k}| \tanh(|\mathbf{k}|h)}$ .

The process of casting the QC transport equation in a form like the RTE results in the introduction of the scattering source term  $S_{qc}$  to the RHS of Equation (5).  $S_{qc}$  accounts for the generation of coherent structures in the wave field due to the interactions of wave components with medium variations. These interactions are considered within the area around  $\mathbf{x}$ , where we consider that the generation of coherent structures occurs. When  $S_{qc}$  is absent from Equation (1) or negligible, the governing equation reduces to the radiative transfer equation and  $W$  to the variance density spectrum.

$$S_{qc} = -i \sum_{q=-q_{max}}^{q=q_{max}} \left[ \Delta \widehat{\Omega}^q(\mathbf{k}, \mathbf{x}, -i\nabla_x) W(\mathbf{k} - \frac{q}{2}, \mathbf{x}, t) \right] + i \sum_{q=-q_{max}}^{q=q_{max}} \left[ \Delta \widehat{\Omega}^{q*}(\mathbf{k}, \mathbf{x}, i\nabla_x) W(\mathbf{k} + \frac{q}{2}, \mathbf{x}, t) \right] \tag{9}$$

$$\Delta \widehat{\Omega}^q(\mathbf{k}, \mathbf{x}, -i\nabla_x) = \Delta \widehat{\sigma}^q - \frac{i}{2} \partial_k \left( \Delta \widehat{\sigma}^q \right) \frac{\mathbf{k}}{|\mathbf{k}|} \nabla_x, \quad \Delta \widehat{\Omega}^{q*} : \text{complex conjugate of } \Delta \widehat{\Omega}^q \tag{10}$$

$\Delta \widehat{\sigma}^q$  represents the Fourier transform  $\Delta \widehat{\sigma}^q = \bar{F}_{\xi, q} \{ \Delta \sigma \}$ , where  $\Delta \sigma$  is the difference between the local dispersion function value and its local plane approximation, following [39], multiplied by a Tukey (tapered cosine) window function:

$$\Delta \sigma = \text{TWF}(\xi) \left[ \sigma(\mathbf{k}, \mathbf{x} + \xi) - \sigma(\mathbf{k}, \mathbf{x}) - \xi \nabla_x \sigma|_{\mathbf{k}, \mathbf{x}} \right] \tag{11}$$

$$\text{TWF}(\xi) = \begin{cases} 0.5(1 + \cos(\pi(\frac{\xi}{l\gamma} - 1))), & 0 \leq \xi < l\gamma \\ 1, & l\gamma \leq \xi < (1 - \gamma)l \\ 0.5(1 + \cos(\pi(\frac{l-\xi}{l\gamma} - 1))), & (1 - \gamma)l \leq \xi < l \end{cases} \quad (12)$$

with  $l = 0.5|\xi_c|$ .

$S_{qc}$  and all its dependencies, like  $\Delta\sigma$ ,  $\Delta\widehat{\sigma^q}$ , and  $\Delta\widehat{\Omega^q}$ , are evaluated in an area of length  $|\xi_c|$  centered around  $\mathbf{x}$ . The resemblance of  $\Delta\widehat{\Omega^q}$  to the first-order QC approximation of Equation (4) is not accidental.  $\Delta\widehat{\Omega^q}$  is the remainder of  $\widehat{\Omega}^{(1)}$  that is not incorporated inside the LHS of the model's governing equation in the process of deriving it from Equation (3). The multiplication of  $\Delta\sigma$  by the Tukey window function is a measure for handling discontinuities that may be encountered near the edges of the coherent footprint area around  $\mathbf{x}$ , wherein  $\Delta\sigma$  is assumed to be a periodic function so that  $\Delta\widehat{\sigma^q}$  can be obtained by the means of a Fourier transform.

### 2.1.2. Model Implementation

For the simulations considered in this study, the steady state form of the governing equation was evaluated (i.e.,  $\partial W/\partial t = 0$ ) using regular, rectilinear spatial and spectral grids, defined as:

$$(\mathbf{x}, \mathbf{y}) = [m_x\Delta x, m_y\Delta y], 0 \leq m_x \leq M_x, 0 \leq m_y \leq M_y, m_x, m_y \in \mathbb{N} \quad (13)$$

$$(\mathbf{k}_x, \mathbf{k}_y) = [n_x\Delta k_x, n_y\Delta k_y], 0 \leq n_x \leq N_x, 0 \leq n_y \leq N_y, n_x, n_y \in \mathbb{N} \quad (14)$$

The discrete form of Equation (3) is obtained by approximating the gradient differential operators with second-order upwind finite differences.

$$\Delta_x^+ W_{\mathbf{k},\mathbf{x}} = \frac{3W_{\mathbf{k},\mathbf{x}} - 4W_{\mathbf{k},\mathbf{x}-\Delta\mathbf{x}} + W_{\mathbf{k},\mathbf{x}-2\Delta\mathbf{x}}}{2\Delta\mathbf{x}}, \Delta_x^- W_{\mathbf{k},\mathbf{x}} = \frac{-3W_{\mathbf{k},\mathbf{x}} + 4W_{\mathbf{k},\mathbf{x}+\Delta\mathbf{x}} - W_{\mathbf{k},\mathbf{x}+2\Delta\mathbf{x}}}{2\Delta\mathbf{x}} \quad (15)$$

$$\Delta_{\mathbf{k}}^+ W_{\mathbf{k},\mathbf{x}} = \frac{3W_{\mathbf{k},\mathbf{x}} - 4W_{\mathbf{k}-\Delta\mathbf{k},\mathbf{x}} + W_{\mathbf{k}-2\Delta\mathbf{k},\mathbf{x}}}{2\Delta\mathbf{k}}, \Delta_{\mathbf{k}}^- W_{\mathbf{k},\mathbf{x}} = \frac{-3W_{\mathbf{k},\mathbf{x}} + 4W_{\mathbf{k}+\Delta\mathbf{k},\mathbf{x}} - W_{\mathbf{k}+2\Delta\mathbf{k},\mathbf{x}}}{2\Delta\mathbf{k}} \quad (16)$$

where Equations (15) and (16) reference points outside the computational grid and the finite-difference schemes revert to first-order accurate ones. The incoming spectrum is applied on the southern geographical boundary, while the northern and lateral geographical boundaries are allowed to be crossed only by outgoing waves that exit the computational domain. The CM spectrum is considered zero outside the spectral computational grid.

The evaluation of  $S_{qc}$  requires at least second-order accurate spatial discretization, as the accounted wave coherence introduces fast spatial scales into the calculations [38]; therefore, second- and fourth-order accurate finite differences were used. The Fourier transforms in Equations (5) and (6) are calculated by a 2D discrete Fourier transform using a fast Fourier transform algorithm [47,48]. Moreover, the evaluation of Equations (5)–(7) requires the definition of an auxiliary spatial grid and its conjugate auxiliary spectral grid. Both are centered around the evaluated geographical and spectral points  $\mathbf{x}$ ,  $\mathbf{k}$  and are defined as:

$$\begin{aligned} \boldsymbol{\xi} &= \mathbf{x} + [m_{x'}\Delta x', m_{y'}\Delta y'], \\ -0.5M_q \leq m_{x'} \leq 0.5M_q, -0.5M_q \leq m_{y'} \leq 0.5M_q, m_{x'}, m_{y'} &\in \mathbb{N} \end{aligned} \quad (17)$$

$$\begin{aligned} \mathbf{q} &= \mathbf{k} + [n_{q_x}\Delta q_x, n_{q_y}\Delta q_y], \\ -0.5M_q \leq n_{q_x} \leq 0.5M_q, -0.5M_q \leq n_{q_y} \leq 0.5M_q, n_{q_x}, n_{q_y} &\in \mathbb{N} \end{aligned} \quad (18)$$

The length of the spatial auxiliary grid equals  $\xi_c$ , which is the length of the assigned coherence radius of the wave field, with the assumption that  $\Delta\mathbf{k} \leq 2\pi/\xi_c$ .

To avoid the interpolation of  $W$  in spectral space,  $\Delta q_i$  is chosen such that  $\Delta q_x = \Delta q_y = 2\Delta k$ , and  $\Delta x'$  is defined as  $\Delta x' = 2\pi/(M_q \Delta q)$ , as per [38]. It is obvious that  $M_q$  is the number of the discrete Fourier components along each direction.  $M_q$  is evaluated by  $\Delta q$  and the choice of an appropriate  $q_{\max}$ , which can be defined as  $q_{\max} \leq a k_{\text{mean}}$ , where  $k_{\text{mean}}$  is the mean wavenumber of the wave field and  $q_{\max} = |q_{\max}|$ .

Solving the discrete form of the governing equation requires  $O(M_x M_y N_x N_y M_q M_q)$  operations. This is due to the operations needed for evaluating  $S_{qc}$ , as solving the LHS of Equation (5) requires  $O(M_x M_y N_x N_y)$  operations. Therefore, the evaluation  $S_{qc}$  is the most computationally intensive part of the governing equation. The choice of  $q_{\max}$  affects the computational time, as the number of  $M_q M_q$  Fourier components is directly affected by this choice. As a result,  $q_{\max}$  and  $M_q$  should be kept as small as possible while at the same time ensuring that the coherent structures and wave interferences are accurately resolved. To that end, we adopted the measures that Smit et al. [39] propose to reduce the factor of  $O(M_q M_q)$  more computations that are needed for  $S_{qc}$ . Setting  $q_{\max}/|k| \leq 2$  for each wavenumber,  $k$ , of the spectral computational grid reduces the number of calculations, helps in preventing erroneous backscattering when calculating  $S_{qc}$  at low wavenumbers and agrees with the limit that the QC approximation sets in the aperture of coherent interactions [35]. In addition,  $S_{qc}$  is computed only for  $|k|h_{\min} \leq 2.3$ , where  $h_{\min}$  is the minimum water depth inside the spatial auxiliary domain  $x'$  that corresponds to the coherent footprint of  $S_{qc}$ . Variations in depth cause small variations in  $\sigma = \sqrt{g|k|\tanh(|k|h)}$  for large wavenumbers, so that  $\Delta\sigma \rightarrow 0$  and  $S_{qc}$  becomes negligible.

Another measure of computational efficiency is the pre-computation of  $\Delta\sigma$  for every spatial grid point before the main part of the solution algorithm. Since the evaluation of  $\sigma$  involves the magnitude  $|k|$  of wavenumber  $k$ , Smit et al. [39] proposed the evaluation of  $\Delta\sigma$  at  $N = 100$  equidistant points between the minimum and maximum  $|k|$  of the spectral grid. The precalculated  $\Delta\sigma$  values are then interpolated on the spectral grid defined by Equation (14). Here, we took this approach a step further and took advantage of the shape of  $\sigma = \sqrt{g|k|\tanh(|k|h)}$ , which is steeper for variations in small-wavenumber magnitudes. To that end, instead of equidistant points, we used logarithmically spaced points between the minimum and maximum  $|k|$ , thus reducing  $N$ .

The described discretization yields a linear equations system that is iteratively solved in a semi-implicit manner, like the one employed in the SWAN wave model [2]. Spectral space is divided in 4 quadrants, where  $Q_1 = \{k_x \geq 0, k_y \geq 0\}$ ,  $Q_2 = \{k_x \leq 0, k_y \geq 0\}$ ,  $Q_3 = \{k_x \geq 0, k_y \leq 0\}$  and  $Q_4 = \{k_x \leq 0, k_y \leq 0\}$ . In each iteration, every point  $x$  is visited in a marching fashion 4 times, 1 time per sweep of the geographical domain. Each sweep is aligned with the propagation directions implied by the wavenumber subset of each quadrant (e.g., from the lower left corner to the upper right corner for quadrant 1). Spatial information is propagated from the downwind points in a Gauss–Seidel manner. This technique breaks down the linear equations system into 4 smaller ones for every point of the spatial grid.

The inclusion of the  $S_{qc}$  term makes the LHS diagonal matrix denser by adding  $M_q^2$  diagonals. The resulting systems are solved using the ILU preconditioned BiCGStab method [49]. The simulations end after  $n$  iterations when the following criterion is met for 99% of the geographical points, following [39]:

$$\frac{\sum_k (W_n^{k,x} - W_{n-1}^{k,x})^2}{\sum_k (W_n^{k,x})^2} \leq \alpha^2, \alpha = 0.01 \tag{19}$$

Smit et al., in their earlier work [38], propose  $\alpha = 10^{-4}$ . We have also used this criterion when conducting earlier simulations of the present study. However, we found that the less strict and more economical criterion, from a computational time viewpoint,  $\alpha = 0.01$ , as in [39], was more than adequate, as the differences in the model results, in terms of the significant wave height  $H_s$ , were unnoticeable.

2.2. Test Cases: Waves Propagating over Elliptic Shoal

The resulting model was used for simulating test cases from the well-known experiments of random waves propagating over a submerged shoal presented in Vincent and Briggs [42]. These included the test cases M2, U3, U4, N3 and N4 from the non-breaking waves series of experiments. Smit and Janssen [35] compared their model results with the observational data of experiments M2 and N4. They additionally considered a modified N4 case with narrower directional spreading of the incident spectrum, which they named N4'. The test cases considered in the present paper are presented in Table 1.

Table 1. Incident spectra for model simulations.

Test Number	Case ID	Type	Period (Tp) (sec)	Height (Hs) (cm)	A	γ (Peakedness Factor)	σ <sub>m</sub> (Directional Spreading) (deg)
1	M2	Monochromatic	1.30	2.54	---	---	---
2	U3	TMA Spectrum	1.30	2.54	0.00155	2	0
3	U4	TMA Spectrum	1.30	2.54	0.00047	20	0
4	N3	TMA Spectrum	1.30	2.54	0.00155	2	30
5	N4	TMA Spectrum	1.30	2.54	0.00047	20	10
6	N4'	TMA Spectrum	1.30	2.54	0.00047	20	3

The incident spectra of cases U3, U4, N3, N4 and N4' are of the TMA shallow-water spectral form (Bouws et al. [50]). Following Vincent and Briggs [42], the TMA frequency spectra were multiplied by the wrapped normal spreading function D(θ) expressed in its Fourier series form so that the directional spectra could be obtained. Since our model is formulated in terms of wavenumber **k** (**k<sub>x</sub>**, **k<sub>y</sub>**), the spectral space, S<sub>TMA</sub>(f,θ), was converted to S<sub>TMA</sub>(**k**).

$$S_{TMA}(f, h) = \alpha g^2 f^{-5} (2\pi)^{-4} \Phi(2\pi f, h) e^{-5/4(\frac{f}{f_m})^{-4}} \gamma \exp[-(\frac{f}{f_m} - 1)^2 / 2\sigma^2] \tag{20}$$

With

$$\Phi(\sigma, h) = \left[ \frac{\mathbf{k}^{-3}(\sigma, h) \frac{\partial \mathbf{k}(\sigma, h)}{\partial \sigma}}{\mathbf{k}^{-3}(\sigma, \infty) \frac{\partial \mathbf{k}(\sigma, \infty)}{\partial \sigma}} \right] \tag{21}$$

$$D(\theta) = \frac{1}{2\pi} + \frac{1}{\pi} \sum_{l=1}^L \exp(-\frac{(l\sigma_m)^2}{2}) \cos l(\theta - \theta_m) \tag{22}$$

$$S(f, \theta) = S(f)D(\theta) \tag{23}$$

$$S(\mathbf{k}) = \frac{S(f, \theta)}{J}, J = 2\pi \mathbf{k} \frac{\partial \sigma}{\partial \mathbf{k}} \tag{24}$$

where θ<sub>m</sub> = mean wave direction at frequency f, L = arbitrary number of Fourier harmonics, σ<sub>m</sub> = directional spreading in degrees, f<sub>m</sub> = peak frequency, α = parameter controlling the total variance density, γ = peakedness factor, and h = local depth.

The spatial computational grid had the same size as the wave basin used in the experiments (30 m × 25 m) with a spatial step of Δx = 0.125 m. The spectral grid extents were (−0.5 k<sub>p</sub>, 3.5 k<sub>p</sub>) in the mean wave direction and (−1.5 k<sub>p</sub>, 1.5 k<sub>p</sub>) in the lateral direction, with **k<sub>p</sub>** being the peak wavenumber and with a resolution of Δk = 0.2 rad/m.

Since Δq = 2Δk, to avoid interpolation on the values of W(**k**, **x**) while computing S<sub>qc</sub>, the selection of Δk directly affects how accurately the coherent effects of the wave field will be resolved by the model. The interdependence of Δk, Δq and ξ<sub>c</sub> ≤ 2π/Δk, as well as the fact that ξ<sub>c</sub> = 2π/Δk<sub>0</sub>, indicates the connection between Δk and the consideration of the characteristic width of the spectrum Δk<sub>0</sub>. Although Smit and Janssen and

Smit et al. [35,38,39] thoroughly examine the relationships between the scales involved the QC approximation, they do not directly quantify what should be an acceptable value for  $\Delta k_0$ , implying that  $\Delta k_0$  could be accepted as equal to  $\Delta k$ . Akrish et al. [40] propose that  $\Delta k = \Delta k_0/s = s_d/s$ , and  $s \geq 1$ , where  $s_d$  is the standard deviation of the spectrum. This is a very reasonable and solid suggestion and is consistent with the QC theory. However, it can lead to a very high resolution in the spectral space when very narrow-banded wave spectra are considered, resulting in very high demands in terms of computational time and resources. On the other hand, the approach of Smit and Janssen and Smit et al. [35,38,39] is more economical at the expense of possibly defining a smaller coherence radius. In the present work, we chose the latter for computational efficiency reasons.

The rationale supporting this decision was that computational speed and efficiency is an important factor in many operational use cases. For example, timely forecasts of wave fields are of the essence when using wave models as components of larger sea-state forecast platforms. Very high grid resolutions could result in simulations that may not be complete in time. In such conditions, it would be mandatory to set a lower threshold to  $\Delta k$  while bearing in mind that it could be larger than the standard deviation of the incident spectrum, if the latter happened to be so narrow-banded that  $s_d < \Delta k$ . Our choice of  $\Delta k = 0.2 \text{ rad/m}$  was larger than the spectrum  $s_d$  of case M2, as is presented in Table 2. Therefore, by using this spectral grid configuration, it would be possible to evaluate the effectiveness and accuracy of our QC model implementation under conditions where  $\Delta k = s_d/s$  and  $s \geq 1$  cannot be satisfied.

**Table 2.** Standard deviation of  $S_{TMA}(k)$  for test cases M2, U3, U4, N3, N4 and N4'. The presented values were calculated considering  $S_{TMA}(k)$  on a  $k$  equidistant grid and after converting  $S_{TMA}(f)$  to a wavenumber spectrum.

Test Number	Case ID	Standard Deviation $s_d$ (m/(rad/m))
1	M2	0.0517
2	U3	1.3019
3	U4	0.7482
4	N3	1.3019
5	N4	0.7482
6	N4'	0.7482

As far as the other parameterizations of our QC model are concerned,  $l = 0.2$  (parameter in the Tukey window function in Equation (12)),  $q_{max} = k_{mean}$ , with  $k_{mean}$  being the mean wavenumber of the incident spectrum, and  $N = 50$  (the number of logarithmically spaced points of the wavenumber magnitude for the pre-calculation of  $\Delta\sigma$ ).

### 3. Results

Apart from the simulations with the QC model, two additional series of simulations were performed for each test case considered. The first one was with our model reduced to its RTE form (i.e.,  $S_{qc} = 0$ ). The second was with the SWAN wave model in the RTE mode, excluding the dissipation of the wave energy (e.g., whitecapping, surf breaking) and any additional processes such as approximations of non-linear wave-wave interactions, the phase-decoupled diffraction approximation, etc. The results of each model (RTE, SWAN) were plotted together and compared with the results of the QC model.

For cases M2, N4 and N4', we also compared our model with the results of Smit and Janssen [35], who used a different model configuration, which will be referred to as QC-SJ13. They solved the first-order QC approximation of Equation (3), not Equation (5), which they approximated with slope-limited second-order accurate finite differences in the spatial and spectral grids combined with an explicit scheme of the first-order finite difference in time. They used periodic boundary conditions for the lateral boundaries and a radiation-type boundary for the northern boundary opposite to the wave-maker. Last, they selected  $q_{max} \leq 2k_p$ , with  $k_p$  being the peak wavenumber.

The results of our simulations are graphically presented in Figures 1–12, where the different model results and laboratory data are intercompared. In addition to the figures produced based on the model results, the differences in the models are presented in a quantitative manner by the calculated Willmott skill scores (WS) presented in Tables 3–5.

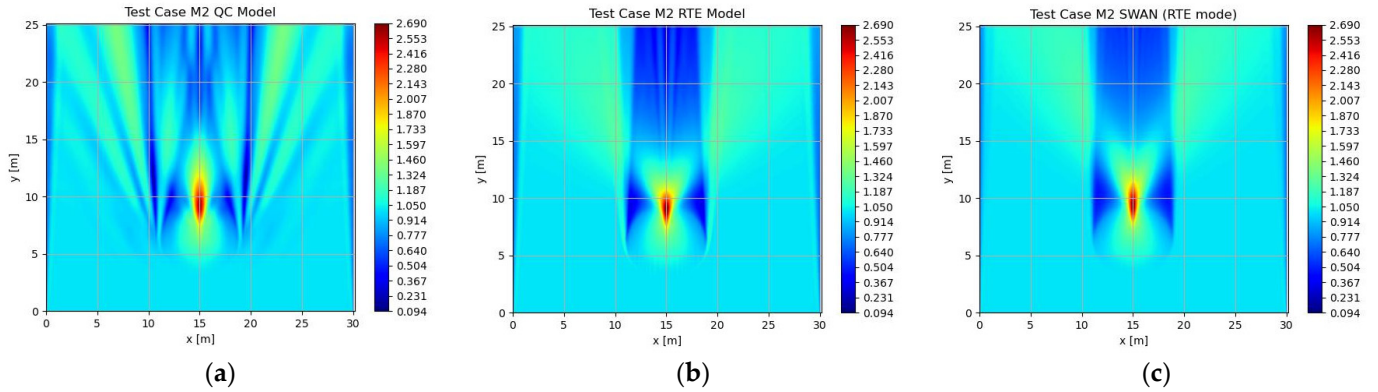


**Figure 1.** Test Case M2: Plan view of simulated normalized wave heights. (a) QC model; (b) RTE model; (c) SWAN wave model in RTE mode.

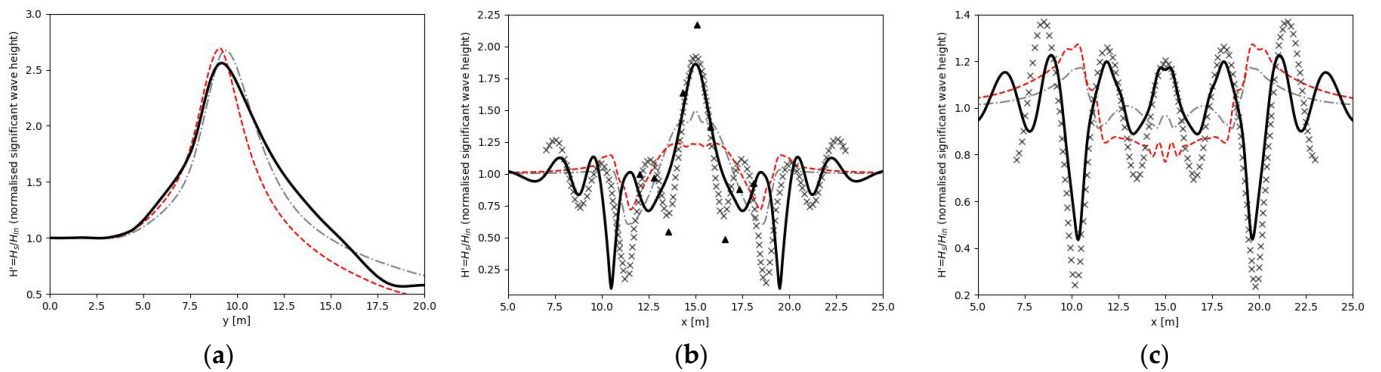


**Figure 2.** Test Case M2: Normalized wave height along transects across and behind the shoal: (a) Transect 7–9 (along  $x = 15$  m); (b) transect 4 (along  $y = 12.19$  m); (c) transect 5 (along  $y = 15.24$  m). QC model: bold black line; RTE model: dashed red line; SWAN wave model: dashed grey line; Observational data along transect 4: triangular markers; QC-SJ13 model: grey ‘x’ markers.

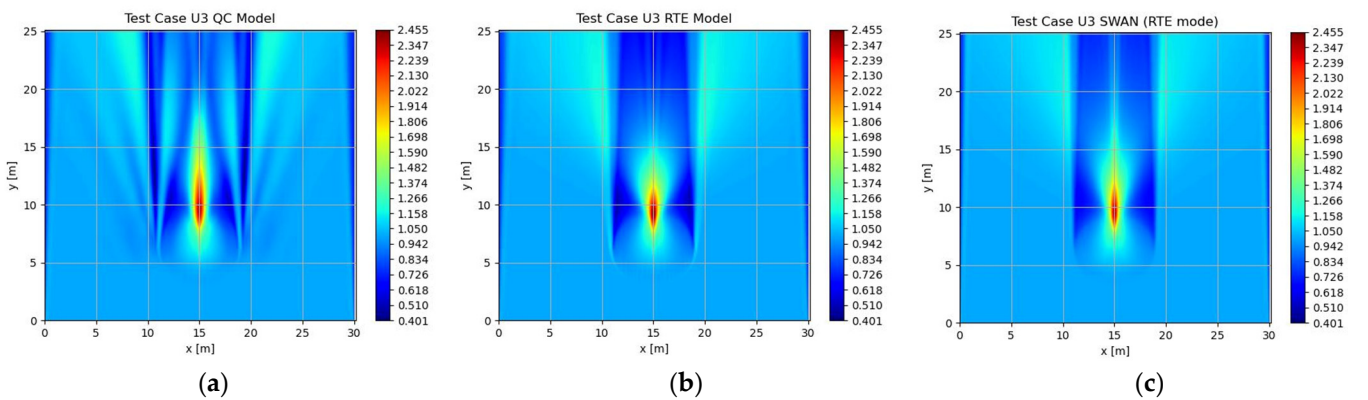


**Figure 3.** Test Case U3: Plan view of simulated normalized wave heights: (a) QC model; (b) RTE model; (c) SWAN wave model in RTE mode.

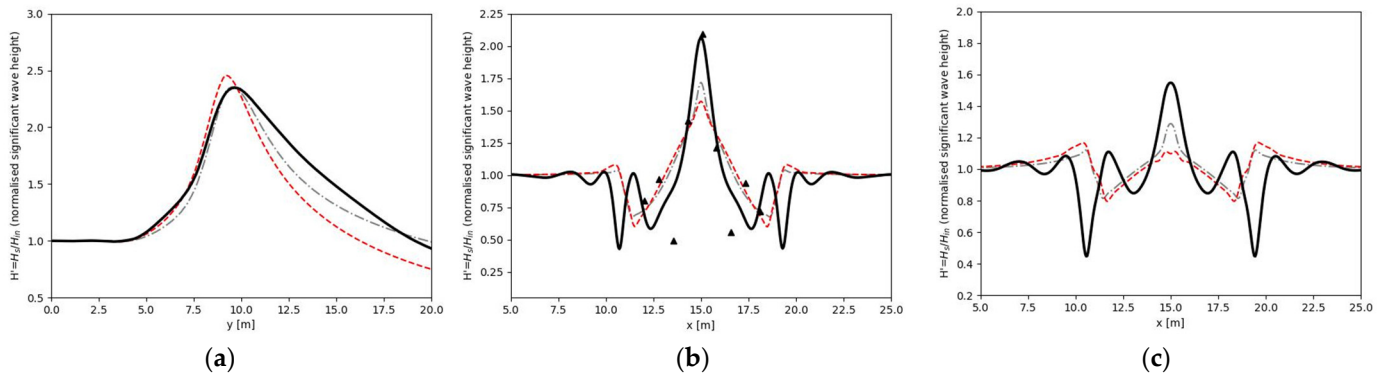


**Figure 4.** Test Case U3: Normalized wave height along transects across and behind the shoal: (a) Transect 7–9 (along  $x = 15$  m); (b) transect 4 (along  $y = 12.19$  m); (c) transect 5 (along  $y = 15.24$  m). QC model: bold black line; RTE model: dashed red line; SWAN wave model: dashed grey line; observational data along transect 4: triangular markers.

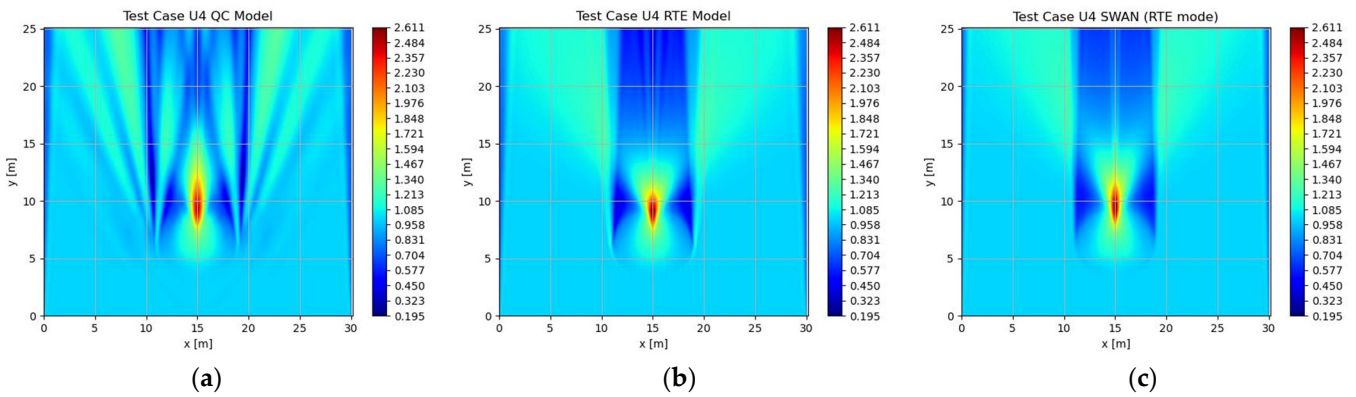


**Figure 5.** Test Case U4: Plan view of simulated normalized wave heights: (a) QC model; (b) RTE model; (c) SWAN wave model in RTE mode.

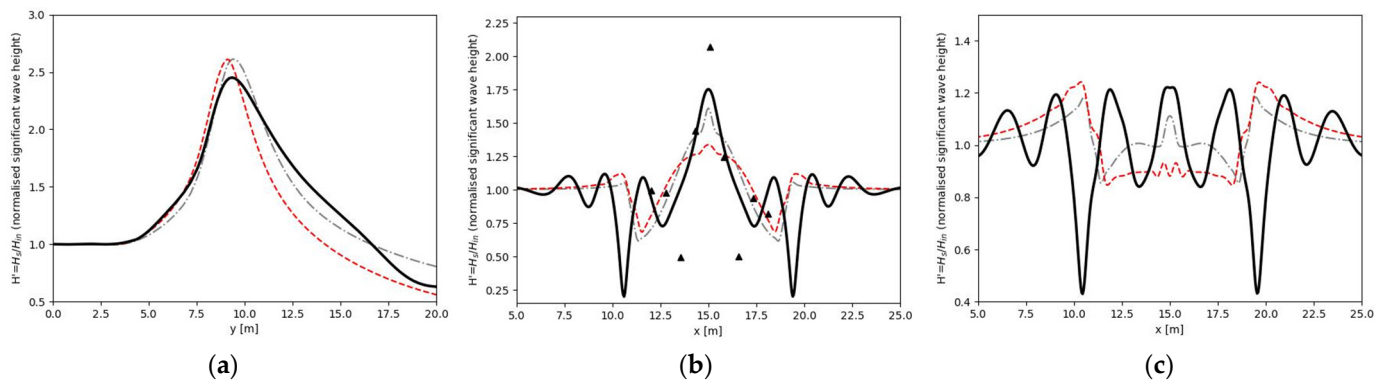


**Figure 6.** Test Case U4: Normalized wave height along transects across and behind the shoal: (a) Transect 7–9 (along  $x = 15$  m); (b) transect 4 (along  $y = 12.19$  m); (c) transect 5 (along  $y = 15.24$  m). QC model: bold black line; RTE model: dashed red line; SWAN wave model: dashed grey line; observational data along transect 4: triangular markers.

The results showed that our implementation of the QC model could approximate the higher significant wave height values detected in the shadow zone behind the shoal, as opposed to the RTE model and SWAN model operating in the RTE mode. The QC results were closer to the available observational data than those of the RTE model. Our version of the QC model confirmed the capability of the quasi-coherent theory to resolve coherent wave interference patterns, unlike the RTE approach. The RTE and SWAN models

tended to predict much stronger focusing over the shoal, especially in the more narrow-banded cases. On the contrary, the QC model could scatter wave components behind the shoal and capture their interference when they crossed, as is evidenced by the alternating lobes of the attenuated and increased wave height. Despite the different configuration, our implementation of the QC theory was in good agreement with the results of Smit and Janssen [35]. The bigger differences between the two sets of results were detected in transect 5. These concerned the magnitude and exact position of the alternating lobes of the simulated normalized wave height and are further discussed in the following section of the present paper.

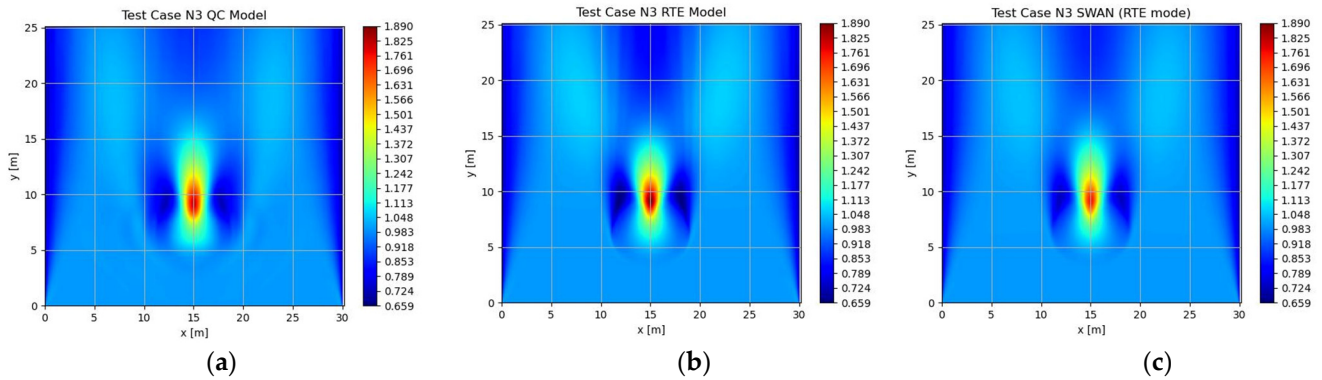


Figure 7. Test Case N3: Plan view of simulated normalized wave heights: (a) QC model; (b) RTE model; (c) SWAN wave model in RTE mode.

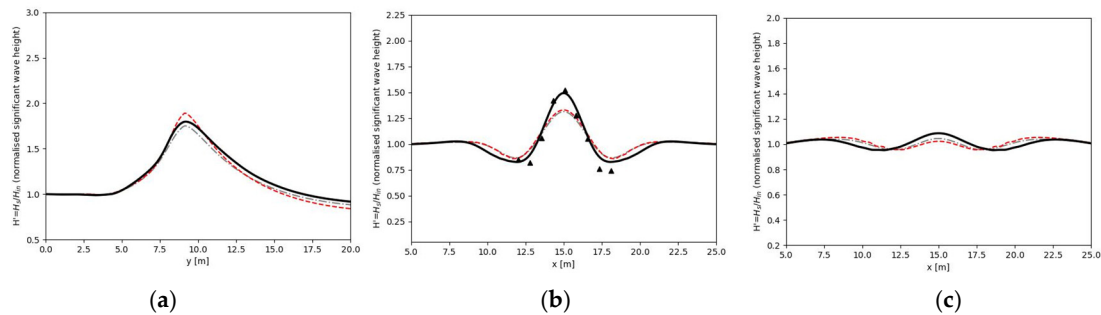


Figure 8. Test Case N3: Normalized wave height along transects across and behind the shoal: (a) Transect 7–9 (along  $x = 15$  m); (b) transect 4 (along  $y = 12.19$  m); (c) transect 5 (along  $y = 15.24$  m). QC model: bold black line; RTE model: dashed red line; SWAN wave model: dashed grey line; observational data along transect 4: triangular markers.

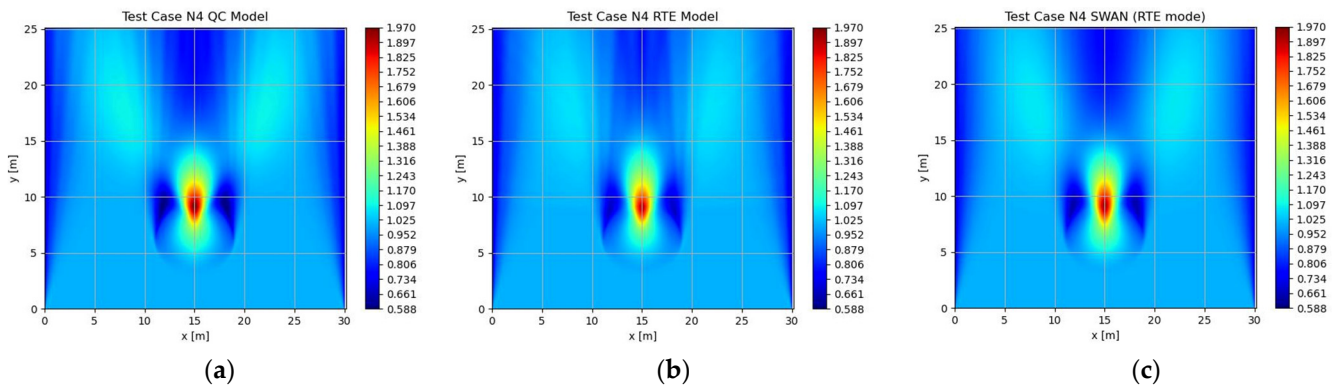
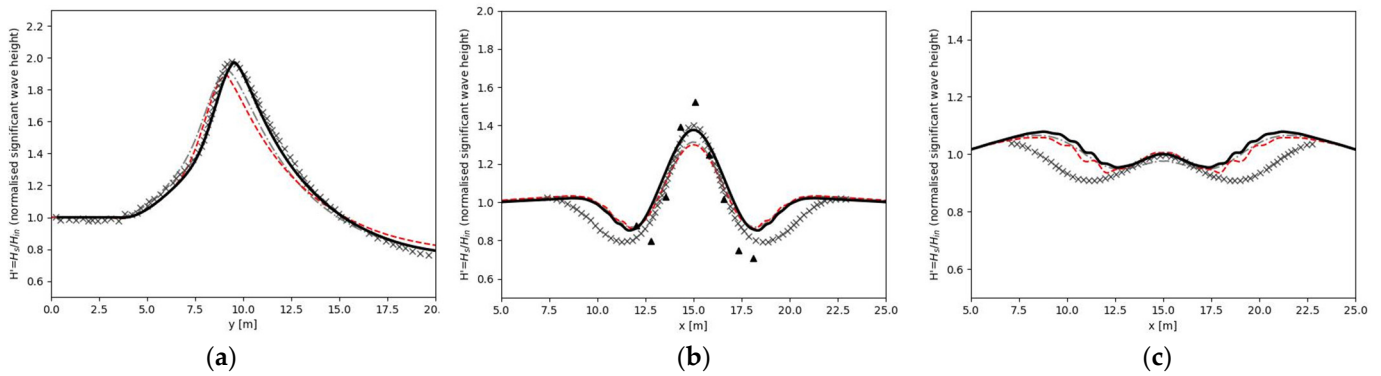
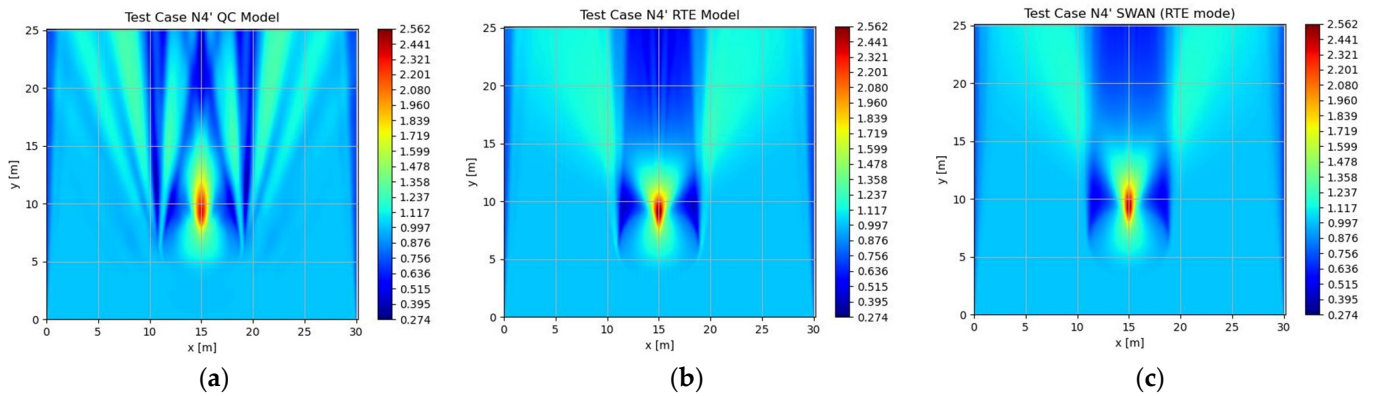


Figure 9. Test Case N4: Plan view of simulated normalized wave heights: (a) QC model; (b) RTE model; (c) SWAN wave model in RTE mode.



**Figure 10.** Test Case N4: Normalized wave height along transects across and behind the shoal (a) Transect 7–9 (along  $x = 15$  m); (b) transect 4 (along  $y = 12.19$  m); (c) transect 5 (along  $y = 15.24$  m). QC model: bold black line; RTE model: dashed red line; SWAN wave model: dashed grey line; observational data along transect 4: triangular markers; QC-SJ13 model: grey ‘x’ markers.



**Figure 11.** Test Case N4': Plan view of simulated normalized wave heights: (a) QC model; (b) RTE model; (c) SWAN wave model in RTE mode.

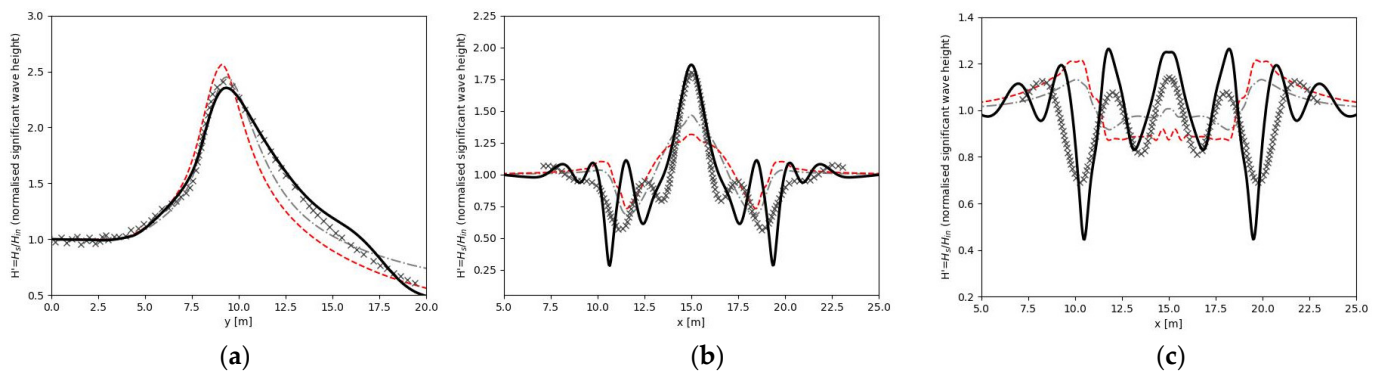


**Figure 12.** Test Case N4': Normalized wave height along transects across and behind the shoal: (a) Transect 7–9 (along  $x = 15$  m); (b) transect 4 (along  $y = 12.19$  m); (c) transect 5 (along  $y = 15.24$  m). QC model: bold black line; RTE model: dashed red line; SWAN wave model: dashed grey line; observational data along transect 4: triangular markers; QC-SJ13 model: grey ‘x’ markers.

In test cases N3 and N4, the QC and RTE models produced similar results, as the broader and more dispersive wave field quickly decorrelated, resulting in smoother wave statistics and no persistent wave interference patterns. Still, the QC model predicted higher wave heights in the shadow zone behind the shoal, which were closer to the observations. Our RTE model and the SWAN model yielded very similar results without capturing interference patterns, as expected.

**Table 3.** Willmott skill score of all models versus laboratory data from Vincent and Briggs for test cases M2, U3, U4, N3 and N4 along transect 4.

Case ID	QC Model of Present Study	Smit and Janssen QC Implementation	RTE Model	SWAN
M2	0.901	0.961	0.395	0.67
U3	0.935	N/A	0.789	0.848
U4	0.851	N/A	0.573	0.756
N3	0.984	N/A	0.966	0.962
N4	0.921	0.964	0.903	0.903

**Table 4.** Willmott skill score of QC model of present study versus Smit and Janssen’s [35] implementation model results for test cases M2, N4 and N4’.

Case ID	Transect 7–9	Transect 4	Transect 5
M2	N/A	0.769	0.658
N4	0.998	0.956	0.373
N4’	0.976	0.922	0.526

**Table 5.** Willmott skill score of RTE model versus SWAN results for test cases M2, N4 and N4’.

Case ID	Transect 7–9	Transect 4	Transect 5
M2	0.972	0.904	0.85
N4	0.997	0.998	0.994
N4’	0.981	0.96	0.908

The findings mentioned above are also supported by the calculated WS scores presented in Tables 3–5.

Small local undershoots of unnatural negative variance density and subsequently significant wave heights were detected in case M2, where the wave height attained the lowest values to the left and right of the shoal. These were probably caused by very large gradients due to the very narrow incident CM spectrum in combination with the selected numerical scheme. The problem was ameliorated by slightly increasing the smoothing effect of the TWF (Equation (16)) in  $S_{qc}$  ( $\gamma = 0.3$  instead of  $\gamma = 0.1$ , as per [31,32]) and using a hybrid scheme of second-order accurate central and first-order upwind finite differences in spectral space.

#### 4. Discussion

The results show that our model can reproduce the findings of the QC theory and modeling framework. Along with the results of [35,38–40], they prove that the QC theory and modeling framework can be valuable tools, allowing a more accurate prediction of the evolution of inhomogeneous wave fields near the coast, where incident waves can be weakly dispersive, as in the case of swells approaching the shore.

Small differences were detected between our results and the results of Smit and Janssen [35], with the latter performing slightly better when compared with the measured laboratory data. The differences mainly consisted of the slightly different magnitudes and exact positions of the alternating lobes of the increased and attenuated wave height, which were evident in transects 4 and 5, perpendicular to the mean direction of the incident waves.

As far as the magnitude of the alternating lobes of the wave height is concerned, our model yielded smaller differences in the wave height between the alternating peaks and troughs in case M2 than those presented in [35]. This can be specifically attributed to the fact that in case M2, we used a TWF formulation with  $\gamma = 0.3$ , which essentially smoothed the effect of  $S_{qc}$ , as a measure of mitigating the emergence of the local numerical undershoots stated in the “Results” section. The opposite occurred in cases N4 and N4’, where we used  $\gamma = 0.1$ .

A more comprehensive explanation about the differences detected between the results of the present study and the ones in [35] should be based on considering the different implementations of the QC theory and the resulting numerical models, both in the terms of the form of their governing equation as well as from the aspect of its numerical solution.

The most apparent difference between the two models, and possibly the most important, is the different form of the governing equation. Equation (3), which is the equation used in [35] and is closer to the analytic mathematical derivation of the evolution of the coupled-mode spectrum  $W(\mathbf{k}, \mathbf{x}, t)$  presented in the same paper, implies that the coherent radius of the wave field covers the entire spatial domain. This means that the evolution of  $W(\mathbf{k}, \mathbf{x}, t)$  depends on medium variations that exist across the entire spatial domain. On the contrary, Equation (5), which is derived from Equation (3) in [38], assumes a finite coherent radius, outside of which the medium variations do not affect the local evolution of  $W(\mathbf{k}, \mathbf{x}, t)$ . The latter is expected in actual sea wave fields from a physical point of view. Moreover, the form of Equation (5) is more practical in terms of numerical evaluation and expansion and has source terms that consider additional physical processes. However, it is possible that Equation (3) might be better suited for approximating the idealized conditions of the series of experiments for non-breaking waves presented in [35].

Drawing definite conclusions regarding the importance of the different numerical approaches is difficult, as [35] leans more heavily on the derivation and presentation of the new theory and less on providing details about its numerical implementation. Regarding the latter, both [35] and the present study use the same spatial grid extent and discretization and the same spectral grid extend. However, the rest of the model configurations are different. Smit and Janssen [35] solved the governing equation (Equation (3)) with an explicit first-order time stepping until a steady state is reached, whereas the present study was based on the stationary equation, i.e., Equation (5).

In [35], Smit and Janssen use periodic boundary conditions on the open lateral boundaries of the geographical computational domain, whereas we chose to use boundaries that were crossed only by outgoing waves leaving the domain. The latter type of conditions is also used in operational spectral wave models, when measured data along the boundaries are insufficient or completely missing. Simulations with the QC model of the present study, albeit with periodic lateral boundary conditions, produced results almost identical to the ones presented in the previous section. Specifically, the wave heights differed only on the lateral boundaries and in zones with a width of a few cells adjacent to the lateral boundaries.

Smit and Janssen [35] mention the use of slope-limited second-order finite differences without describing the formulation of the slope limiter or the exact type of finite differences. Additionally, [35] mentions that  $\Delta\mathbf{k}/k_p = [16,18]$  instead of explicitly stating the spectral grid discretization of their simulations. The simulations of the present study were carried out by employing  $Dk = 0.2$  rad/m and SORDUP finite differences, except for test case M2, where a hybrid scheme of SORDUP and second-order central finite differences were used. The lack of a more detailed description of the numerical scheme and the spectral grid resolution in [35] hinders a safe further analysis about the impact of these apparent differences on the results of both models that implement the QC theory.

However, the differences in the results of the present QC model and the one in [35] are not contradictory, as both solutions support the predictions of the theory they implement. After all, similar differences were also detected between our RTE model and SWAN, which differ in terms of the governing equation formulation, as the former is based on Equation (1) and the latter on Equation (2). Both cases demonstrate the greater importance of the theoretical framework supporting each modelling approach rather than the specific implementation of each separate numerical model. This could be further investigated in the future by trying to reproduce the results from Smit et al. in [38] and [39], as the same governing equation is used, and our solution algorithm was more based on the works presented in those papers.

Choosing a spectral resolution with  $\Delta k$  being relatively larger than the standard deviation of a very narrow incident spectrum, but simultaneously not too coarse, did not inhibit the model from resolving the coherent interference patterns, as the results demonstrated for test case M2. Therefore, using somewhat less strict criteria for defining the spectral grid resolution in favor of computational speed and resource efficiency, when necessary for operational use cases, did not cancel the QC model's advantages over the classic RTE models, nor did it produce results contradicting the QC theory. On another note, possible local undershoots that lead to unnatural results due to very narrow spectra can be prevented, without sacrificing accuracy, by selecting appropriate and numerical schemes and TWF formulation. However, research for future improvements may also include further study about numerical schemes, diminishing the possibility of undershoots without resorting to ad hoc measures like increasing the smoothing effect of TWF on  $S_{qc}$ .

## 5. Conclusions

Overall, the model implementation in the present work forms a sound basis for using the QC theory to simulate the evolution of inhomogeneous wave fields that interact with a variable topography. As such, it can be used as a means for future research on aspects regarding further advances in the QC modeling framework and theory. In addition, it can also serve as a starting point for investigating the benefits of its potential use in more operational use cases by incorporating existing extensions (surf breaking, wave–current interaction) and providing the means for testing new ones.

**Author Contributions:** Conceptualization, V.B.; methodology, V.B.; software, V.B.; validation, V.B.; formal analysis, V.B.; investigation, V.B.; resources, V.B.; data curation, V.B.; writing—original draft preparation, V.B.; writing—review and editing, Y.N.K.; visualization, V.B.; supervision, Y.N.K. All authors have read and agreed to the published version of the manuscript.

**Funding:** This research received no external funding.

**Institutional Review Board Statement:** Not applicable.

**Informed Consent Statement:** Not applicable.

**Data Availability Statement:** Not applicable.

**Conflicts of Interest:** The authors declare no conflict of interest.

## References

1. The WAMDI Group. The WAM model—A third generation ocean wave prediction model. *J. Phys. Oceanogr.* **1988**, *18*, 1775–1810. [[CrossRef](#)]
2. Booij, N.; Ris, R.C.; Holthuijsen, L.H. A third-generation wave model for coastal regions 1. Model description and validation. *J. Geoph. Res. Oceans* **1999**, *104*, 7649–7666. [[CrossRef](#)]
3. Tolman, H.L. A third-generation model for wind waves on slowly varying, unsteady, and inhomogeneous depths and currents. *J. Phys. Oceanogr.* **1991**, *21*, 782–797. [[CrossRef](#)]
4. Amarouche, K.; Akpınar, A.; Bachari, N.E.I.; Çakmak, R.E.; Houma, F. Evaluation of a high-resolution wave hindcast model SWAN for the West Mediterranean basin. *Appl. Ocean. Res.* **2019**, *84*, 225–241. [[CrossRef](#)]
5. Mentaschi, L.; Besio, G.; Cassola, F.; Mazzino, A. Performance evaluation of Wavewatch III in the Mediterranean Sea. *Ocean. Model.* **2015**, *90*, 82–94. [[CrossRef](#)]
6. Hoque, M.A.; Perie, W.; Solomon, S.M. Application of SWAN model for storm generated wave simulation in the Canadian Beaufort Sea. *J. Ocean. Eng. Sci.* **2020**, *5*, 19–34. [[CrossRef](#)]
7. Makris, C.; Androulidakis, Y.; Karambas, T.; Papadimitriou, A.; Metallinos, A.; Kontos, Y.; Baltikas, V.; Chondros, M.; Krestenitis, Y.; Tsoukala, V.; et al. Integrated modelling of sea-state forecasts for safe navigation and operational management in ports: Application in the Mediterranean Sea. *Appl. Math. Model.* **2021**, *89*, 1206–1234. [[CrossRef](#)]
8. Copernicus Marine Environment Monitoring Service, Providing PRODUCTS and SERVICES for All Marine Applications. Available online: <https://marine.copernicus.eu/> (accessed on 30 July 2023).
9. Poseidon System: Monitoring, Forecasting and Information System for the Greek Seas. Available online: <https://poseidon.hcmr.gr/> (accessed on 30 July 2023).
10. WaveForUs: A Pilot System for the Development and Delivery of Daily Wave and Circulation Forecasts for Public and Emergency Use in the Thermaikos Gulf. Available online: <https://wave4us.web.auth.gr/> (accessed on 30 July 2023).

11. Rusu, L.; Soares, C.G. Evaluation of a high-resolution wave forecasting system for the approaches to ports. *Ocean Eng.* **2013**, *58*, 224–238. [[CrossRef](#)]
12. Anton, I.A.; Rusu, L.; Anton, C. Nearshore wave dynamics at Mangalia Beach simulated by spectral models. *J. Mar. Sci. Eng.* **2019**, *7*, 206. [[CrossRef](#)]
13. Cavaleri, L.; Abdalla, S.; Benetazzo, A.; Bertotti, L.; Bidlot, J.-R.; Breivik, Ø.; Carniel, S.; Jensen, R.E.; Portilla-Yandun, J.; Rogers, W.E.; et al. Wave modelling in coastal and inner seas. *Prog. Oceanogr.* **2018**, *167*, 164–233. [[CrossRef](#)]
14. Cavaleri, L.; Alves, J.G.; Ardhuin, F.; Babanin, A.V.; Banner, M.L.; Belibassakis, K.; Benoit, M.; Donelan, M.A.; Groeneweg, J.; Herbers, T.H.; et al. Wave Modelling—The State of the Art. *Prog. Oceanogr.* **2007**, *75*, 603–674. [[CrossRef](#)]
15. Liu, Q.; Gramstad, O.; Babanin, A. Kinetic equations in a third-generation spectral wave model. *J. Fluid Mech.* **2021**, *910*, A50. [[CrossRef](#)]
16. Karambas, T.; Koutitas, C. A breaking wave propagation model based on the Boussinesq equations. *Coast. Eng.* **1992**, *18*, 1–19. [[CrossRef](#)]
17. Karambas, T.; Memos, C. Boussinesq model for weakly nonlinear fully dispersive water waves. *J. Water. Port. Coast. Ocean Eng.* **2009**, *135*, 187–199. [[CrossRef](#)]
18. Auclair, F.; Bordois, L.; Dossmann, Y.; Duhaut, T.; Paci, A.; Ulses, C.; Nguyen, C. A non-hydrostatic non-Boussinesq algorithm for free-surface ocean modelling. *Ocean. Model.* **2018**, *132*, 12–29. [[CrossRef](#)]
19. Lannes, D. Modeling shallow water waves. *Nonlinearity* **2020**, *33*, R1–R57. [[CrossRef](#)]
20. Mei, C.C. The applied dynamics of ocean surface waves. *Adv. Ser. Ocean. Eng.* **1994**, *1*, 86–89. [[CrossRef](#)]
21. Dingemans, M.W. Water wave propagation over uneven bottoms. *Adv. Ser. Ocean. Eng.* **1997**, *13*. [[CrossRef](#)]
22. Porter, D. The mild-slope equations. *J. Fluid Mech.* **2003**, *494*, 51–63. [[CrossRef](#)]
23. Melito, L.; Antuono, M.; Brocchini, M. From Boussinesq-type to quasi-3D models: A comparative analysis. *J. Hydr. Eng.* **2023**, *149*, 04023025. [[CrossRef](#)]
24. Antuono, M.; Brocchini, M. Beyond Boussinesq-type equations: Semi-integrated models for coastal dynamics. *Phys. Fluids* **2013**, *25*, 016603. [[CrossRef](#)]
25. Dimas, A.A.; Fialkowski, L.T. Large-Wave Simulation (LWS) of Free-Surface Flows Developing Weak Spilling Breaking Waves. *J. Comp. Phys.* **2000**, *159*, 172–196. [[CrossRef](#)]
26. Leftheriotis, G.A.; Chalmoukis, I.A.; Oyarzun, G.; Dimas, A.A. A Hybrid Parallel Numerical Model for Wave-Induced Free-Surface Flow. *Fluids* **2021**, *6*, 350. [[CrossRef](#)]
27. Agnon, Y.; Sheremet, A. Stochastic nonlinear shoaling of directional spectra. *J. Fluid Mech.* **1997**, *345*, 79–99. [[CrossRef](#)]
28. Herbers, T.H.C.; Burton, M.C. Nonlinear shoaling of directionally spread waves on a beach. *J. Geoph. Res. Oceans* **1997**, *102*, 101–114. [[CrossRef](#)]
29. Herbers, T.H.C.; Orzech, M.; Elgar, S.; Guza, R.T. Shoaling transformation of wave frequency—Directional spectra. *J. Geoph. Res. Oceans* **2003**, *108*, 3013. [[CrossRef](#)]
30. Alber, I.E. The effects of randomness on the stability of two—Dimensional surface watertrains. *Philos. T. Roy. Soc.* **1978**, *A 363*, 525–546. [[CrossRef](#)]
31. Janssen, P.A.E.M. Long-time behaviour of a random inhomogeneous field of weakly nonlinear surface gravity waves. *J. Fluid Mech.* **1983**, *133*, 113–132. [[CrossRef](#)]
32. Janssen, T.T. Nonlinear Surface Waves over Topography. Ph.D. Dissertation, Delft University of Technology, Delft, The Netherlands, 2006.
33. Janssen, T.T.; Herbers, T.H.C.; Battjes, J.A. Evolution of ocean wave statistics in shallow water: Refraction and diffraction over seafloor topography. *J. Geoph. Res. Oceans* **2008**, *113*, C03024. [[CrossRef](#)]
34. Stiassnie, M.; Regev, A.; Agnon, Y. Recurrent solutions of Alber’s equation for random water-wave fields. *J. Fluid Mech.* **2008**, *598*, 245–266. [[CrossRef](#)]
35. Smit, P.B.; Janssen, T.T. The evolution of inhomogeneous wave statistics through a variable medium. *J. Phys. Oceanogr.* **2013**, *43*, 1741–1758. [[CrossRef](#)]
36. Cohen, L. *Time-Frequency Analysis*; Prentice-Hall Signal Processing: Hoboken, NJ, USA, 1995.
37. Cohen, L. Phase-Space Differential Equations for Modes. In *Pseudo-Differential Operators: Complex Analysis and Partial Differential Equations. Operator Theory: Advances and Applications*; Schulze, B.W., Wong, M.W., Eds.; Birkhäuser Basel: Basel, Switzerland, 2009; Volume 205. [[CrossRef](#)]
38. Smit, P.B.; Janssen, T.T.; Herbers, T.H.C. Stochastic modeling of coherent wave fields over variable depth. *J. Phys. Oceanogr.* **2015**, *45*, 1139–1154. [[CrossRef](#)]
39. Smit, P.B.; Janssen, T.T.; Herbers, T.H.C. Stochastic modeling of inhomogeneous ocean waves. *Ocean. Model.* **2016**, *96*, 26–35. [[CrossRef](#)]
40. Akrish, G.; Smit, P.; Zijlema, M.; Reniers, A. Modelling statistical wave interferences over shear currents. *J. Fluid Mech.* **2020**, *891*, A2. [[CrossRef](#)]
41. Akrish, G.; Smit, P.; Zijlema, M.; Reniers, A. A mild-slope formulation based on Weyl rule of association with application to coastal wave modelling. *Wave Motion* **2023**, *122*, 103189. [[CrossRef](#)]
42. Vincent, C.L.; Briggs, M.J. Refraction—Diffraction of Irregular Waves over a Mound. *J. Wat. Port Coast. Ocean Eng* **1989**, *115*, 269–284. [[CrossRef](#)]

43. Gabor, D. Theory of Communication. Part1: The analysis of information. *J. Inst. Electr. Eng.* **1946**, *93*, 429–441. [[CrossRef](#)]
44. Mandel, L.; Wolf, E. *Optical Coherence and Quantum Optics*; Cambridge University Press: Cambridge, UK, 1995. [[CrossRef](#)]
45. Bastiaans, M.J. Application of the Wigner distribution function in optics. In *The Wigner Distribution—Theory and Applications in Signal Processing*; Mecklenbräuker, W., Hlawatsch, F., Eds.; Elsevier: Amsterdam, The Netherlands, 1997; pp. 375–426.
46. Bastiaans, M.J. Transport Equations for the Wigner Distribution Function. *Opt. Acta Int. J. Opt.* **1979**, *26*, 1265–1272. [[CrossRef](#)]
47. Swarztrauber, P.N. FFT algorithms for vector computers. *Parallel Comput.* **1984**, *1*, 45–63. [[CrossRef](#)]
48. Frigo, M.; Johnson, S. The Design and Implementation of FFTW3. *Proc. IEEE* **2005**, *93*, 216–231. [[CrossRef](#)]
49. Van der Vorst, H.A. Bi-CGSTAB: A Fast and Smoothly Converging Variant of Bi-CG for the Solution of Nonsymmetric Linear Systems. *SIAM J. Sci. Stat. Comput.* **1992**, *13*, 631–644. [[CrossRef](#)]
50. Bouws, E.; Gunther, H.; Rosenthal, W.; Vincent, C.L. Similarity of the wind wave spectrum in finite depth water1. Spectral form. *J. Geoph. Res.-Ocean.* **1985**, *90*, 975–986. [[CrossRef](#)]

**Disclaimer/Publisher’s Note:** The statements, opinions and data contained in all publications are solely those of the individual author(s) and contributor(s) and not of MDPI and/or the editor(s). MDPI and/or the editor(s) disclaim responsibility for any injury to people or property resulting from any ideas, methods, instructions or products referred to in the content.